Fully biodegradable and self-powered nerve guidance conduit based on zinc-molybdenum batteries for peripheral nerve repair

Bingbing Yu [a,1], Jun Bai [b,e,h,1], Yanjun Guan [b,e,1], Xueying Huang [a], Lijing Liang [b], Zhiqi Ren [b], Xiangyu Song [b,c], Tieyuan Zhang [b,d], Can Yang [a], Fanqi Dai [a], Xibo Wang [a], Xing Sheng [e], Jiang Peng [b,f], Liu Wang [g,**], Yu Wang [b,f,***], Lan Yin [a,*]

[a] School of Materials Science and Engineering, The Key Laboratory of Advanced Materials of Ministry of Education, State Key Laboratory of New Ceramics and Fine Processing, Laboratory of Flexible Electronics Technology, Tsinghua University, Beijing, 100084, China
[b] Institute of Orthopedics, The Fourth Medical Center of Chinese PLA General Hospital, Beijing Key Lab of Regenerative Medicine in Orthopedics, Key Laboratory of Musculoskeletal Trauma & Injuries PLA, Beijing, 100048, China
[c] Hebei North University, Zhangjiakou, 075051, China
[d] Shandong University Center for Orthopedics, Cheeloo College of Medicine, Shandong University, Jinan, 250012, China
[e] Department of Electronic Engineering, Beijing National Research Center for Information Science and Technology, Institute for Precision Medicine, Laboratory of Flexible Electronics Technology, and IDG/McGovern Institute for Brain Research, Tsinghua University, Beijing, 100084, China
[f] Co-innovation Center of Neuroregeneration, Nantong University, Nantong, Jiangsu Province, 226007, China
[g] Key Laboratory of Biomechanics and Mechanobiology of Ministry of Education, Beijing Advanced Innovation Center for Biomedical Engineering, School of Biological Science and Medical Engineering, and with the School of Engineering Medicine, Beihang University, Beijing, 100083, China
[h] Department of Neurosurgery, Xuanwu Hospital, Capital Medical University, Beijing, 100053, China

A B S T R A C T

Peripheral nerve injury (PNI) poses a significant public health issue, often leading to muscle atrophy and persistent neuropathic pain, which can drastically impact the quality of life for patients. Electrical stimulation represents an effective and non-pharmacological treatment to promote nerve regeneration. Yet, the postoperative application of electrical stimulation remains a challenge. Here, we propose a fully biodegradable, self-powered nerve guidance conduit (NGC) based on dissolvable zinc-molybdenum batteries. The conduit can offer topographic guidance for nerve regeneration and deliver sustained electrical cues between both ends of a transected nerve stump, extending beyond the surgical window. Schwann cell proliferation and adenosine triphosphate (ATP) production are enhanced by the introduction of the zinc-molybdenum batteries. In rodent models with 10-mm sciatic nerve damage, the device effectively enhances nerve regeneration and motor function recovery. This study offers innovative strategies for creating biodegradable and electroactive devices that hold important promise to optimize therapeutic outcomes for nerve regeneration.

1. Introduction

Peripheral nerve injury (PNI) represents a severe problem in public health, resulting from various causes such as falls, vehicle crashes, industrial accidents, and neurodegeneration associated with chronic diseases (Noble et al., 1998). PNI often leads to muscle atrophy and persistent neuropathic pain, and in more severe cases, may cause irreversible impairment to sensory or motor functions (Feinberg et al., 1997; Kemp et al., 2017). Trauma-related PNI accounts for 2–5 percent of patients admitted to level I trauma facilities in the United States,

creating a significant clinical burden (Taylor et al., 2008). End-to-end anastomosis has been used for treating small segments of nerve defects. However, tension-free surgical sutures are not available for large lesion gaps (>5 mm), for which reconstructive grafts are needed (Johnson and Soucacos, 2008). Currently, autologous nerve grafting is widely accepted as the "gold standard" for treating large segmental defects in clinical settings. However, its application is limited by the scarcity of donor tissues, functional damage at donor sites, and the requirement for secondary surgical procedures (Meena et al., 2021). The development of diverse and functional artificial nerve conduits have attracted great interests as they offer an alternative strategy to autograft techniques and has demonstrated promise to enhance tissue regeneration (Carvalho et al., 2019).

Electrical stimulation represents a widely employed non-pharmacological technique for rehabilitation, pain relief, neuromodulation, and nerve repair (Lee et al., 2022; Gordon and English, 2016; Wang et al., 2022). Bioelectrical signals change when acute and chronic nerve injuries happen (Isaacson and Bloebaum, 2010), and appropriate electrical cues can help regulate the bioelectric microenvironment at the injured site, inhibit synaptic stripping and alleviate neuropathic pain, so as to promote nerve regeneration and ameliorate dysfunction (Chu et al., 2022; Casella et al., 2021). Both alternating current (AC) stimulation and direct current (DC) electric fields have demonstrated significant therapeutic effects for nerve regrowth. For AC stimulation, factors such as the frequency, intensity, and pattern of electrical stimulation are taken into account (Meng, 2014), and biphasic stimulation with frequency at 20 Hz and pulse widths between 50 and 500 μs is often employe (Adams et al., 2017; Zhao et al., 2020a; Guo et al., 2021; Frederick et al., 2021). In the case of DC stimulation, electric field intensities between 30 and 80 mV/mm have been reported to enhance neuronal differentiation in PC12 cells (Jing et al., 2019), and both the neurite growth and the secretion of nerve growth factors of Schwann cells are significantly increased under a 50 mV/mm electric field (Koppes et al., 2011, 2014). The time frame of electrical stimulation represents another impact factor on nerve regeneration. It has been demonstrated that applying electrical stimulation for 6 days (1 h per day) or 10 days (15 min per day) after sciatic nerve injury results in faster nerve regeneration and improved muscle function recovery compared to just 1 h of stimulation (Koo et al., 2018; Kong et al., 2024). Similar positive outcomes have been observed in the regeneration of injured facial nerves (Sun et al., 2024). These studies offer evidence supporting the beneficial effects of longer-term electrical stimulation compared to short-term intraoperative stimulation. Although the exact mechanics are not entirely understood, electrical stimulation at the early stage of nerve injuries has been shown to accelerate Wallerian degeneration (Li et al., 2022), modulate the microenvironment and modulate the phenotype of macrophages to reduce local inflammation (McLean and Verge, 2016), increase calcium activity and activates extracellular signal regulating kinase pathways (Guo et al., 2021; Mar et al., 2014), upregulate the expression of neurotrophic factors in Schwann cells (Wan et al., 2010), and promote the elongation of regenerated neurites, thus promoting nerve regeneration (Gordon and English, 2016).

Although intraoperative electrical stimulation has shown effectiveness in clinical practice (Gordon, 2016), maintaining continuous electrical stimulation beyond the timeframe of surgery remains a challenge. Thus, the development of miniaturized and easily deployable electrical stimulators for peripheral nerve regeneration can enhance existing protocols by maximizing therapeutic benefits. Strategies involve inductive coupling, piezoelectricity (Mao et al., 2022; Yang et al., 2023), triboelectricity (Jin et al., 2021), glucose fuel cells (Sun et al., 2019), and primary batteries (Wang et al., 2020; Li et al., 2023) as power sources for electrical stimulation. Further advancement is achieved by the introduction of biodegradable materials, eliminating retraction procedures and unnecessary materials retention (Guo et al., 2021; Koo et al., 2018; Choi et al., 2020; Meng et al., 2023; Zheng et al., 2016; Shan et al., 2024; Li et al., 2024; Yu et al., 2024). Among proposed strategies, electrical

cues provided by biodegradable batteries possess unique advantages, including miniaturization, stable voltage output, and ease of deployment without dependence on external equipment. While magnesium batteries have demonstrated significant efficacy in promoting nerve regeneration, it poses challenges with severe side reactions due to its bioactivity, limiting the operational lifetime of magnesium batteries (Wang et al., 2020). The rapid production of excess hydrogen during operation may also have negative effects on surrounding tissues. In comparison, using zinc as an alternative material for anodes can mitigate these side reactions, extending the operational lifetime of the battery (Lei et al., 2022; Huang et al., 2023; Yin et al., 2014a). The development of biodegradable zinc batteries has shown promise in addressing these challenges. A reported discharging time of 19 days demonstrates the capability of these batteries to effectively power electronic medical devices for extended periods, highlighting their potential in the field of electronic medicine (Huang et al., 2023). Zinc is also an important trace element in human body, playing an important role in biological process. The recommended dietary allowance (RDA) is 8 mg/day for women and 11 mg/day for men (Institute of Medicine Panel on M, 2001). The electrical dissolution rate of zinc is 0.3 ± 0.2 μm h^{-1} in Hank's solutions (Yin et al., 2014b). Nevertheless, the therapeutic efficacy of fully biodegradable zinc batteries on nerve regrowth remains unexplored.

Here we propose a fully biodegradable and self-powered nerve guidance conduit (NGC) based on zinc-molybdenum (Zn-Mo) batteries. The zinc electrodes are fabricated by room temperature sintering to form a conductive network so as to get larger specific surface area and higher operational voltage compared with batteries based on foil electrodes. Molybdenum is selected as the cathode mainly for its biodegradability, biocompatibility and desirable electrode potential (Yin et al., 2014a; Huang et al., 2018). The RDA of molybdenum is 45 μg/day and the tolerable upper intake level (UL) is 2 mg/day (Institute of Medicine Panel on M, 2001). The electrical dissolution rate of molybdenum is (7 ± 4) $\times 10^{-4}$ μm h^{-1} in Hank's solutions (pH = 7.4) at 37 °C (Yin et al., 2014b). The innermost part of the NGC contains a thin layer of aligned polycaprolactone (PCL) fibers, which provide topographical cues to guide the directional growth of axons and the arrangement of Schwann cells (Xie et al., 2014). Moreover, randomly oriented PCL fibers are utilized as the outer layer of the conduit to provide mechanical support and prevent potential deformations that could hinder nerve repair. The biodegradable copolymer of poly (L-lactic acid) and poly (trimethylene carbonate) (PLLA-PTMC) is selected as the middle layer for its soft mechanical properties, providing a desirable interface for nerve tissues (Wang et al., 2020). The presence of the zinc battery significantly enhances the proliferation and adenosine triphosphate (ATP) production of Schwann cells, which is beneficial for nerve regrowth. The self-powered NGC accelerates nerve regeneration and improves motor function recovery in Sprague-Dawley (SD) rats with 10 mm sciatic nerve defects. The materials and fabrication strategy can provide new avenues to achieve sustained electric fields for nerve regeneration.

2. Materials and methods

2.1. Fabrication of zinc and molybdenum electrodes

Zinc particles of 50 nm (Deco Island Gold, China) were mixed with isopropyl (IPA) with a w/v ratio of 1:2 to achieve zinc slurries. Zinc slurries (2 μL) were cast on the surface of a polytetrafluoroethylene (PTFE) mold, and PTFE tapes were used to confine the shape of zinc electrodes (1 × 3 mm). Acetic acid solution (Shanghai Macklin Biochemical Co., Ltd, China) (10%) was then uniformly added onto the surface of zinc slurries. The electrochemical sintering happened from the surface to the interior of the slurries and therefore a slight warping was formed on the sintered sheet. After about 30 min, the acetic acid solution was completely dried and the electrode can be easily released from the PTFE mold. Molybdenum slurries were achieved by mixing

molybdenum particles of 2 μm (Deco Island Gold, China) with poly (lactic-co-glycolic) acid (PLGA) and acetone with a w/v radio of 6:1:10. Molybdenum slurries (20 μL) were drop-casted in the PTFE mold to form molybdenum films (10 × 3 mm), which were subsequently cut into molybdenum slices (1 × 3 mm).

2.2. Fabrication of self-powered NGC

The fully biodegradable and self-powered NGC consisted of multiple layers, including aligned PCL fibers (~30 μm), PLLA-PTMC (~50 μm), zinc and molybdenum electrodes (~100 μm), PLLA-PTMC (~300 μm) and randomly oriented PCL fibers (~200 μm), from the inside out. Both aligned and random PCL fibers were prepared by electrospinning. The electrospinning solution was achieved by dissolving PCL particles in hexafluoroisopropanol (HFP) with a w/v ratio of 1:10. For aligned fibers, solution was drawn from a needle with a 0.4 mm inner diameter at a mass flow rate of 0.06 mL/min; a positive voltage of 16 kV was applied to the needle and a negative voltage of −3 kV was set to the rotating collector (850 rpm). For random fibers, solution was drawn from a needle with a 0.86 mm inner diameter at a mass flow rate of 0.11 mL/min; the positive voltage applied to the needle was the same as above and the negative voltage set to the rotating collector (540 rpm) was −6 kV. PLLA-PTMC films were fabricated by drop-casting. PLLA-PTMC with a ratio of 60/40 was dissolved in chloromethane (CHCl$_3$) with a w/v ratio of 1:10, followed by casting and curing for 12 h at 4 °C. The assembly of the device was achieved by the method shown in Fig. 1c. Zinc and molybdenum electrodes were placed on the two sides of PLLA-PTMC substrate when the solvent was not completely dry. Then an encapsulation layer of PLLA-PTMC was covered on the electrodes to ensure a desirable operational time frame. Electro-spun aligned PCL layer was placed on the top and the planar multilayer structure was rolled up on a PTFE wire with a diameter of 1.5 mm to achieve the device with a 3D tubular shape. An additional electro-spun random PCL layer was wrapped around the device to fix the tubular shape.

2.3. Characterization of materials microstructure, mechanical properties, permeability, electrochemical characteristics and biodegradability

The morphology of materials surface was observed by a field-emission scanning electron microscopy (SEM) system (Zeiss, Belin, Germany). The mechanical properties were evaluated by a universal testing machine (WDW3020, Kexin Co. Ltd., China) with a sample size of 10 × 30 mm at a strain rate of 10 mm/min. The feasibility of mass transport was assessed using a permeability chamber. A composite material consisting of a layer of PLLA-PTMC (300 μm) and a layer of electro-spun PCL fibers (200 μm) was inserted between two compartments of the chamber. The upper compartment contained phosphate-buffered saline (PBS), while deionized water was placed in the lower compartment. After the setup was incubated in a water bath at 37 °C for 24 h, the ion conductivity in the lower compartment was measured using a conductivity meter (KedidaCT3031, China). To meet the volume requirement of the conductivity measurement, the sampled solution was diluted to three times its original volume. The performance of the zinc-molybdenum battery was evaluated by a multichannel battery testing system (Neware, Shenzhen China). The discharge behavior of the self-powered device was carried out in normal saline (0.9 wt% NaCl,
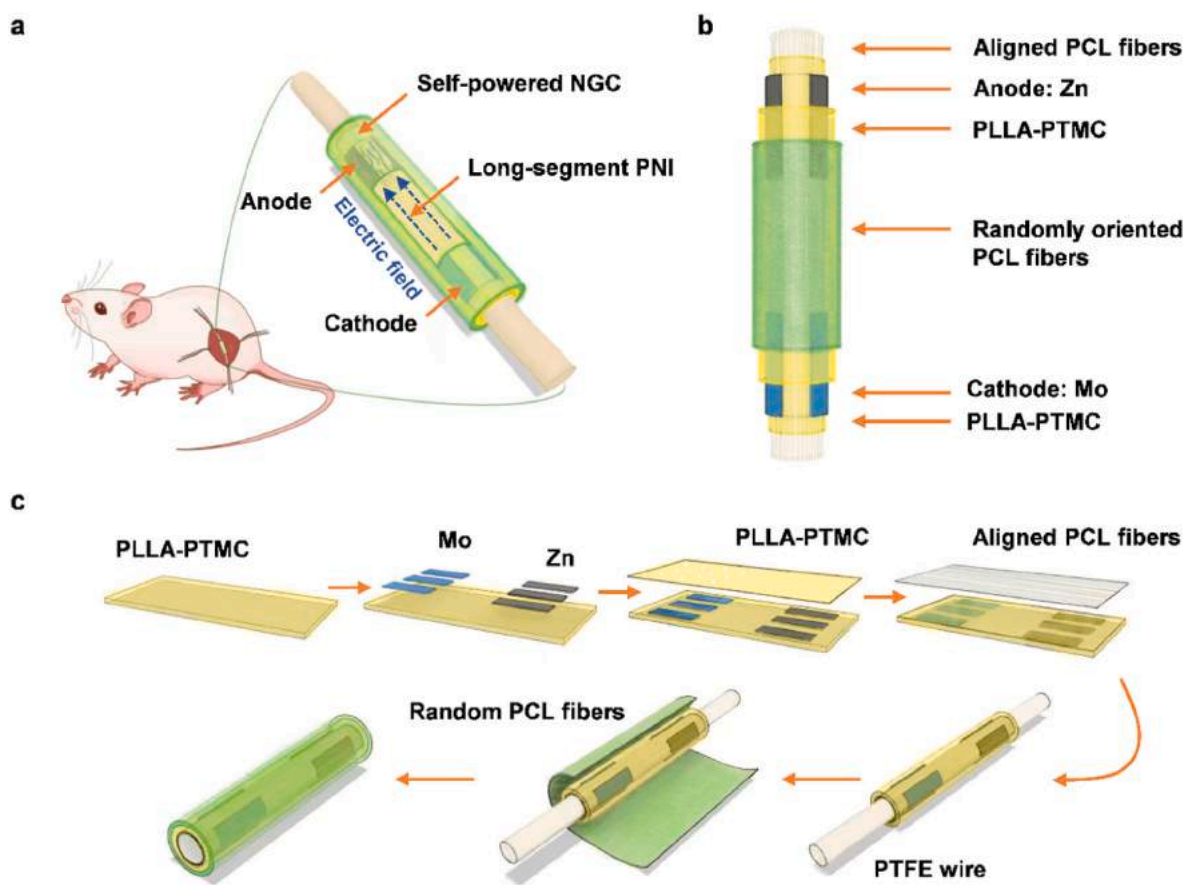

Fig. 1. A fully biodegradable and self-powered NGC as electronic neuroregenerative medicine. a. Schematic illustration of the self-powered NGC for sciatic nerve regeneration. **b.** Schematic exploded illustration of the structure of the device. Structure form inside out: an aligned PCL film for guidance (~20 μm), a PLLA-PTMC film as the encapsulation layer for the zinc-molybdenum battery (~50 μm), a zinc-molybdenum battery (~100 μm), a PLLA-PTMC layer as the substrate (~300 μm), a randomly oriented PCL film for mechanical support (~200 μm). **c.** Fabrication process of the self-powered NGC.

Leagene Biotechnology, China) at a discharge current of 25 μA/cm². The electrodes were connected to copper wires by silver paste and the connections were encapsulated by 3140 RTV Coating (Dow Corning Corp., MI, USA) to stabilize the electrical contact. Batteries based on metallic particles or foils were also investigated with normal saline at a discharge current of 10 μA/cm². The electrical conductivity of PLLA-PTMC after soaking in PBS for 1 h was tested by electrochemical impedance spectroscopy in the frequency range from 1 MHz to 10 Hz by a potentiostat (Interface 1000 E, Gamry, USA). The conductivity is calculated by the following equation

$$\sigma = \frac{l}{RA}$$

where l is the thickness of polymer film, R is the bulk resistance where the impedance data intersects the real axis, and A is the area of the film.

The biodegradation experiments were performed by immersing the planar device in PBS in a water bath. The initial temperature was 37 °C and the temperature was increased to 65 °C after seven days. Time-series images were taken at various stages.

2.4. In vitro studies with Schwann cells

Schwann cells were obtained and purified as described previously (Bai et al., 2023; Lu et al., 2018). Then they were cocultured with metallic electrodes in four different groups as follows: control group (only PLLA-PTMC films), battery group (zinc and molybdenum battery with PLLA-PTMC encapsulation), Zn group (only zinc electrode with PLLA-PTMC encapsulation) and Mo group (only molybdenum electrode with PLLA-PTMC encapsulation). For battery group, zinc slurries (1 μL, zinc: IPA = 1 g: 3 mL) and molybdenum slurries (1 μL, Mo: PLGA: Acetone = 6 g: 1 g: 10 mL) were drop-casted onto the glass coverslips with a distance of 8 mm, and acetic acid solution (10%) was used to sinter the zinc electrode. PLLA-PTMC in CHCl$_3$ (10%) (10 μL) were added to the surface of zinc and molybdenum electrodes for encapsulation. For Zn group and Mo group, the dosage of each electrode was 0.5 μL to ensure a consistent metallic amount with the battery group. Only PLLA-PTMC solution was used in the control group without metallic electrodes. Schwann cells were then seeded onto the 24-well plate with a density of 6000 cells per well and co-cultured for 2 days and 5 days respectively. Cell proliferation was evaluated on day 2 and day 5 using the Cell Counting Kit-8 (CCK-8) (CA1210, Solarbio) and the ATP production of Schwann cells was measured on day 5 using ATP Assay Kit (S0027, Beyotime).

2.5. Surgical procedure

Experimental protocols were approved by the Experimental Animal Ethics Committee of Chinese PLA General Hospital (approval number: 2016-x9-07). All procedures followed the institutional guidelines of the Chinese PLA General Hospital. Female SD rats were randomly divided into three groups, including battery (self-powered NGC with zinc-molybdenum battery), autograft and hollow (nerve conduit without battery) (n = 3 for each group for week 3 evaluation and n = 5 for each group for week 12 evaluation). SD rats were weighted and then anesthetized with pentobarbital sodium (1.5%, 0.3 mL/100 g) via abdominal cavity injection. The sciatic nerve of the right hind leg was exposed by the incision of skin and muscle to create a 10 mm nerve defect. The two stumps of the damaged nerve were then connected by the self-powered NGCs (battery group) and the normal conduits without the battery (hollow group) using 10–0 tension-free band sutures. For the autograft group, the defects were bridged by the excised original nerves. Finally, the operative wounds were closed using 4-0 sutures, and the incision was disinfected with iodine to avoid infection. All rats were then housed in cages with food and water and were subjected to a 12-h light/dark cycle.

2.6. Immunohistochemical assessment of regenerated nerve

Animals in each group were sacrificed by intraperitoneal injection of overdosed pentobarbital sodium solution (n = 3 for each group at week 3 and n = 5 for each group at week 12). Nerve tissues of the injured sides were removed and then fixed with 4% paraformaldehyde (PFA). Samples were dehydrated with a 30% concentration of sucrose solution and subsequently embedded with optimal cutting temperature (OCT) compound gel. Tissues were cut into sections with a thickness of 12 μm using a frozen slicer (Leica, Wetzlar, Germany), longitudinally for tissues collected at week 3 and transversely for tissues collected at week 12. Sections were incubated with goat serum for 30 min. After blocking with goat serum, pathology sections were incubated with primary antibodies at 4 °C overnight. After washing with PBS, the sections were then incubated with secondary antibodies for 2 h at room temperature, protected from light. Primary antibodies used in immunofluorescence staining experiments included mouse anti-NF200 (N0142, Sigma, USA) and rabbit anti-S100β (ab52642, Abcam, USA), and secondary antibodies included goat anti-rabbit Alexa Fluor 594 (ab150080, Abcam, USA) and goat anti-mouse Alexa Fluor 488 (ab150117, Abcam, USA). The DNA was finally stained for 10 min using 4', 6-diamidino-2-phenylindole (DAPI) staining solution (AR1176, BOSTER, USA). Fluorescent images were collected using a confocal panoramic scanner (Pannoramic, 3DHISTECH, Hungary).

2.7. Histological and transmission electron microscopy (TEM) evaluation of myelinated nerve fibers

Regenerated nerves (2 mm) were collected at the distal end at 12 weeks postoperatively. Samples were fixed with 2.5% glutaraldehyde solution for 3 h and 1% osmium tetroxide solution for 1 h, followed by washing, dehydration and embedding. Transverse sections of nerve segments of 2.5 μm in thickness were prepared and stained with toluidine blue dye, and images were observed under a confocal panoramic scanner (Pannoramic, 3DHISTECH, Hungary). Transverse ultrathin sections of nerve segments of 70 nm in thickness were stained with 3% lead citrate and uranyl acetate, and observed by TEM (CM-120, PHILIPS, Netherlands). The myelinated nerve fiber density was quantified from the toluidine blue images and the diameter and G-ratio of myelinated nerve fibers as well as myelin sheath thickness were quantified from TEM images by ImageJ software (Wayne Rasband National Institutes of Health, USA). Hemotoxylin and Eosin (H&E) staining was also carried out at 12 weeks with one-half of the transverse section of regenerated nerves, and images were observed under a confocal panoramic scanner (Pannoramic, 3DHISTECH, Hungary).

2.8. Electrophysiological evaluation

Rats were anesthetized and the sciatic nerve at the injured side was exposed at 12 weeks postoperatively. A multichannel physiological signal acquisition and processing system (RM6240EC, Chengyi) was used to evaluate the compound motor action potentials (CMAPs). The stimulating electrodes were placed at the proximal end of the injured nerve, and the recording electrodes were positioned parallel to the corresponding gastrocnemius muscle. Electrical stimulation (0.3 mA, 200 μs) was applied through the stimulating electrodes to the proximal end of injured nerve and the CMAPs were recorded at the gastrocnemius muscle. The latencies and peak amplitudes of CMAPs were analyzed and compared among three different groups.

2.9. Gastrocnemius muscle evaluation

The rats were sacrificed at 12 weeks postoperatively, by intraperitoneal injection of overdosed pentobarbital sodium solution and the gastrocnemius muscles of both the injured and contralateral sides were harvested and weighted. The wet weight ratio was calculated by

dividing the mass of the injured side by the mass of the contralateral side. The gastrocnemius muscle was then fixed in 4% PFA, followed by dehydration in a graded ethanol series and embedded in paraffin blocks. Transverse sections of 5 μm in thickness were prepared for Masson's trichrome staining. Imaging of the stained sections were observed under a confocal panoramic scanner (Pannoramic, 3DHISTECH, Hungary). The cross-sectional area of the gastrocnemius muscle fibers was quantified by ImageJ software.

2.10. Gait analysis

The motor function recovery was evaluated by the CatWalk XT 10.6

gait analysis system (Noldus, Wageningen, the Netherlands) at 2, 4, 6, 8, 10, 12 weeks postoperatively. The walking trajectory of rats was captured by a camara and analyzed to calculate the sciatic function index (SFI). Three parameters were measured for both the normal side (N) and the injured side (E), including the toe width (TS), intermediate toe width (ITS) and print length (PL). And then the SFI was calculated using the formula as follows: SFI = 109.5 (ETS - NTS)/NTS – 38.3 (EPL - NPL)/NPL + 13.3 (EIT - NIT)/NIT – 8.8.

2.11. Statistical analysis

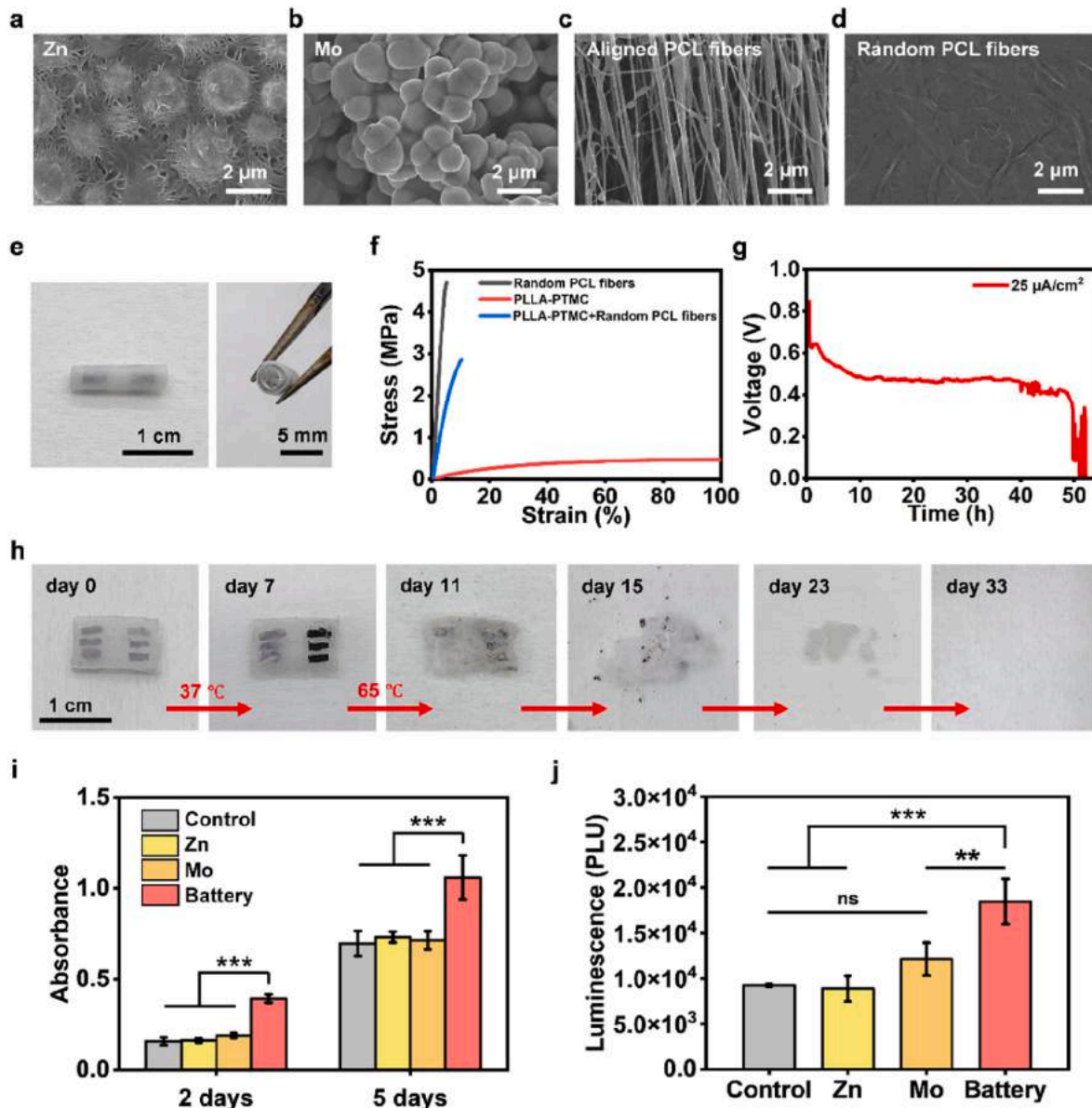Data are given as mean $\pm$ standard deviation. SPSS (IBM, USA) was

Fig. 2. Characterization of the self-powered NGC and evaluation of the influence of the zinc-molybdenum battery on the behavior of Schwann cells. a. SEM image of the zinc electrode. **b.** SEM image of the molybdenum electrode. **c.** SEM image of aligned PCL fibers for structural guidance. **d.** SEM image of randomly oriented PCL fibers for mechanical support. **e.** Optical photos of self-powered NGC: front view (left) and side view (right). **f.** Mechanical properties of the randomly oriented PCL film (elastic modulus: 132.7 $\pm$ 16.2 MPa), PLLA-PTMC film (elastic modulus: 1.19 $\pm$ 0.04 MPa), and the bi-layer composite (elastic modulus: 36.2 $\pm$ 0.57 MPa). **g.** Discharge behavior of zinc-molybdenum battery in normal saline with a discharge current density of 25 μA/cm^2 **h.** Degradation process of the device in PBS (37 °C in the first week and 65 °C afterwards). **i.** Growth behavior of Schwann cells after co-culturing with the PLLA-PTMC substrates (control group), zinc electrodes (Zn group), molybdenum electrodes (Mo group) and the zinc-molybdenum battery (battery group) for 2 days and 5 days. n = 4 independent experiments for each group. **j.** ATP production of Schwann cells after co-culturing with the PLLA-PTMC substrates (control group), zinc electrodes (Zn group), molybdenum electrodes (Mo group) and the zinc-molybdenum battery (battery group) for 5 days. n = 3 independent experiments for each group. The SPSS software package (version 27.0) was used for the statistical analysis, followed by one-way ANOVA (**P < 0.01, ***P < 0.001).

used for analysis of variance (ANOVA) and independent *t*-test analysis. *P<0.05, **P<0.01, ***P<0.001, with "ns" representing no statical difference.

3. Results and discussion

3.1. Materials and fabrication of the self-powered NGC

The schematic structure of the fully biodegradable and self-powered NGC is shown in Fig. 1a, with the exploded illustration in Fig. 1b and the fabrication process in Fig. 1c. The device is comprised of multi-layer biodegradable polymeric films and biodegradable batteries to provide electrical cues and topographical guidance. The polymeric films consist of aligned PCL fibers, PLLA-PTMC layers, and randomly oriented PCL fibers (Fig. 1b). The biodegradable battery is fabricated between the PLLA-PTMC layers, consisting of zinc and molybdenum electrodes. The self-powered NGC is fabricated in the planar format and subsequently rolled into a conduit structure (Fig. 1c). Studies have indicated that the application of electrical stimulation between both ends of a transected nerve stump can effectively improve therapeutic efficacy (Sun et al., 2019; Li et al., 2023; Zhao et al., 2020b). The electrical voltage offered by the Zn-Mo battery is applied at the two ends of the transected nerve, and the nerve gap is considered as a high impedance load. A uniform distribution of electric field intensity is expected along the conduit, as reported previously (Wang et al., 2020).

Specifically, zinc particles are sintered at room temperature to achieve the anodes of the battery. As a thin layer of oxide is often present on the surface of zinc particles due to spontaneously oxidation, which greatly affects the conductivity of zinc particles, acetic acid is therefore introduced to remove the oxide layer. The dissolution of zinc and the redeposition of zinc ions occur simultaneously with the flow of acetic acid between zinc particles, resulting in a porous network (Lee et al., 2017; Jayasayee et al., 2020). The morphology of zinc electrodes before and after sintering is demonstrated in Fig. 2a and Fig. S1a. The molybdenum electrode serves as the cathode and is achieved by drop-casting of slurries consisting of molybdenum particles, PLGA and acetone. Due to the binding of PLGA, molybdenum particles are interconnected to form a 3D network (Fig. 2b). Zinc and molybdenum electrodes fabricated on PLLA-PTMC with a tubular shape are shown in Fig. S1b.

The biodegradable battery is sandwiched between two PLLA-PTMC films. The inner PLLA-PTMC layer (~50 μm) is created for encapsulation to prolong the lifetime of the battery by limiting the side reaction of zinc electrodes and control the releasing rate of zinc and molybdenum ions to ensure biocompatibility. The electrical conductivity of PLLA-PTMC soaked in PBS is 0.71 ± 0.06 mS/cm (Fig. S1c), which is close to most solid polymer electrolytes and some polymer-based gel electrolytes (Yang et al., 2024; Di Pietro and Mele, 2021). These results indicate that the encapsulation PLLA-PTMC layer on the electrode surface will not impede battery discharge performance and passivate the electric pathway. Mini-holes are made in this layer to allow the release of hydrogen potentially generated during the discharging of the battery and therefore avoiding blister formation. Both electrodes are segmented into three separate islands, with a size of 1×3 mm and a spacing of 1 mm between them. This configuration is expected to minimize the internal stress on the electrodes caused by conduit rolling, preventing potential cracking and maintaining optimal conductivity. A layer of electro-spun aligned PCL fibers is incorporated as the innermost layer for structural guidance, while a layer of randomly oriented PCL fibers is wrapped around the outermost of the device for mechanical support. The SEM images represented in Fig. 2c–d and Figs. S1d–e display the surface topography of electro-spun PCL fibers. The inner layer of PCL fibers has an average diameter of 129 ± 62 nm, while the outer layer exhibits randomly oriented fibers, with some entangled fibers possibly resulting from the rapid mass flow rate. The optical images of the device are shown in Fig. 2e. The self-powered device has an inner diameter of approximately 1.5 mm, a size consistent with prior research. In contrast,

the outer diameter of the conduit is around 3 mm, slightly larger than that of typical NGCs (usually 2–2.5 mm) due to the fabrication method utilized for constructing zinc and molybdenum electrodes. Although we did not observe significant mechanical stress on the sutured nerve after implantation, smaller nerve conduits are more advantageous to cause less tension at the sutured sites. The development of alternative fabrication methods to further decrease the size of self-powered NGC represents an interesting future direction.

The mechanical properties of the self-powered device are investigated by tensile experiments and the results are given in Fig. 2f. The PLLA-PTMC film is flexible and highly stretchable, providing a soft interface in contact with nerve tissues. The film of randomly orientated PCL fibers has a much greater elastic modulus, providing desirable modulus to avoid the deformation of NGC when implanted in rats. The composite of PLLA-PTMC and PCL films can therefore offer both soft interfaces and mechanical support. The feasibility of mass transport through the multilayer conduit is assessed using a permeability chamber (Fig. S2). The ion conductivity of the receiving deionized water changes from 0 to 0.057 ± 0.072 mS/cm after 24 h at 37 °C, indicating that ion exchange is possible through the composite film.

The electrical performance of the zinc-molybdenum battery is evaluated by constant current discharging. The anodic reaction proceeds with metal dissolution ($Zn \rightarrow Zn^{2+} + 2e^-$), and the cathodic reaction involves either hydrogen evolution ($2H_2O + 2e^- \rightarrow H_2 + 2OH^-$) or oxygen reduction ($O_2 + 2 H_2O + 4e^- \rightarrow 4OH^-$). The discharge behavior of the battery in normal saline is shown in Fig. 2g. Zinc-molybdenum batteries demonstrate an output voltage around 0.5 V with a discharge current density of 25 μA/cm^2 for 50 h. There are still some electrode materials left after the discharge test, as electrical connection for readout often fails before the complete degradation of materials. The output voltage of zinc-molybdenum batteries based on particles are ~0.15 V higher than that based on foil electrodes (Fig. S3), which is attributed to their large effective surface area. Particle-sintered electrodes exhibit reduced charge transfer resistance and enhanced mass transfer efficiency, leading to improved reaction rates (Huang et al., 2023). The increased surface area provides more active sites for reactions, contributing to overall battery performance. Furthermore, the large surface area of these electrodes plays a crucial role in minimizing concentration changes at the electrode surface resulting from chemical reactions. This reduction in concentration polarization helps sustain the discharge behavior of the battery at a high operational voltage, ensuring desirable efficiency and performance. Moreover, the in vitro life time of the zinc-molybdenum battery is around six times longer than that of the battery based on magnesium-(iron-manganese alloy) electrodes for peripheral nerve repair (Wang et al., 2020), at the same discharge current density of 25 μA/cm^2. The prolonged time frame of electrical cues offered by the zinc-molybdenum battery could be beneficial to enhance therapeutic outcomes (Koo et al., 2018).

The biodegradability of the biodegradable NGC is investigated by soaking the device in PBS (pH = 7.4). Optical images of various stages of the degradation process are shown in Fig. 2h. The degradation is performed at 37 °C for the first 7 days, and some changes of the opaqueness of the device surface were observed probably due to hydrolysis. The temperature is raised to 65 °C after day 7 to accelerate the degradation process, and the device completely dissolves after ~33 days.

3.2. In vitro cell behavior cultured with zinc-molybdenum batteries

Schwann cells represent a type of active glial cell in the peripheral nervous system, which secrete neurotrophic factors and contribute to myelin sheath formation, playing a crucial role in neuron survival and axonal regeneration (Monk et al., 2015). To assess the biocompatibility and potential functionality of zinc-molybdenum batteries, Schwann cells are co-cultured with the battery and electrode materials. In the battery group, zinc and molybdenum electrodes are drop-casted using particle slurries on glass slides, with a thin layer of PLLA-PTMC as the

encapsulation to regulate the release rate of metallic ions. Zn and Mo groups involve individual electrodes made of zinc and molybdenum slurries (with the same PLLA-PTMC encapsulation) respectively are adopted to study the influence of separated effects of each electrode. In the control group, only PLLA-PTMC films are involved.

The growth behavior of Schwann cells is evaluated by the CCK-8 assay. Results show that the proliferation of Schwann cells is significantly promoted in the presence of zinc-molybdenum battery compared with other groups on day 2 and the day 5 (Fig. 2i), consistent with the previously reported results (Wang et al., 2020; Huang et al., 2023). The electrode materials remain intact on day 5, indicating the stability of the battery through the timeframe of cell studies. Moreover, given that enhanced ATP levels are essential for supporting various cellular functions, including proliferation and migration, which can in turn promote nerve regeneration (Bai et al., 2023; Carthew, 2021), the ATP production capacity of Schwann cells is also evaluated using an ATP assay kit. The results demonstrate that the ATP production of Schwann cells in the battery group is significantly greater than that in other groups (Fig. 2j), suggesting that the presence of zinc-molybdenum batteries could promote cell metabolism. This result is in accordance with the previous reports that electrical stimulation can activate the release of calcium ions (Ca^{2+}), and thus induces mitochondrial matrix Ca^{2+} accumulation and increases tricarboxylic (TCA) activity, consequently augmenting

mitochondrial ATP synthesis (Díaz-Vegas et al., 2019). In addition, electrical stimulation of rat sciatic nerve has been reported to increase extracellular ATP levels and induces Ca^{2+} increases in the cytosol and the mitochondrial matrix of surrounding Schwann cells, thus supporting the myelination process (Ino et al., 2015). These in vitro results altogether indicate the beneficial effects of zinc-molybdenum batteries for nerve regeneration.

3.3. Nerve regeneration in rodents with the self-powered NGC

Self-powered NGCs (battery group), autografts (autograft group) and hollow nerve conduits without batteries (hollow group) are implanted to bridge a 10 mm defect of sciatic nerves in SD rats to evaluate the efficacy on peripheral nerve repair (Fig. S4a). Immunofluorescent staining is carried out to investigate the leading edge of regenerated axons at 3 weeks postimplantation, and the density of axons and Schwann cells at 12 weeks postimplantation. Representative results of the longitudinal sections of regenerated nerve tissues at week 3 are shown in Fig. 3a. The white dotted line represents the proximal end of the regenerated nerve, while the yellow line indicates the leading edge of the regenerated axons. The length of regenerated axons is analyzed and the results are given in Fig. 3b. The axonal length in the battery group (8.43 ± 0.44 mm) is significantly greater than that in the hollow group (5.93 ± 1.13
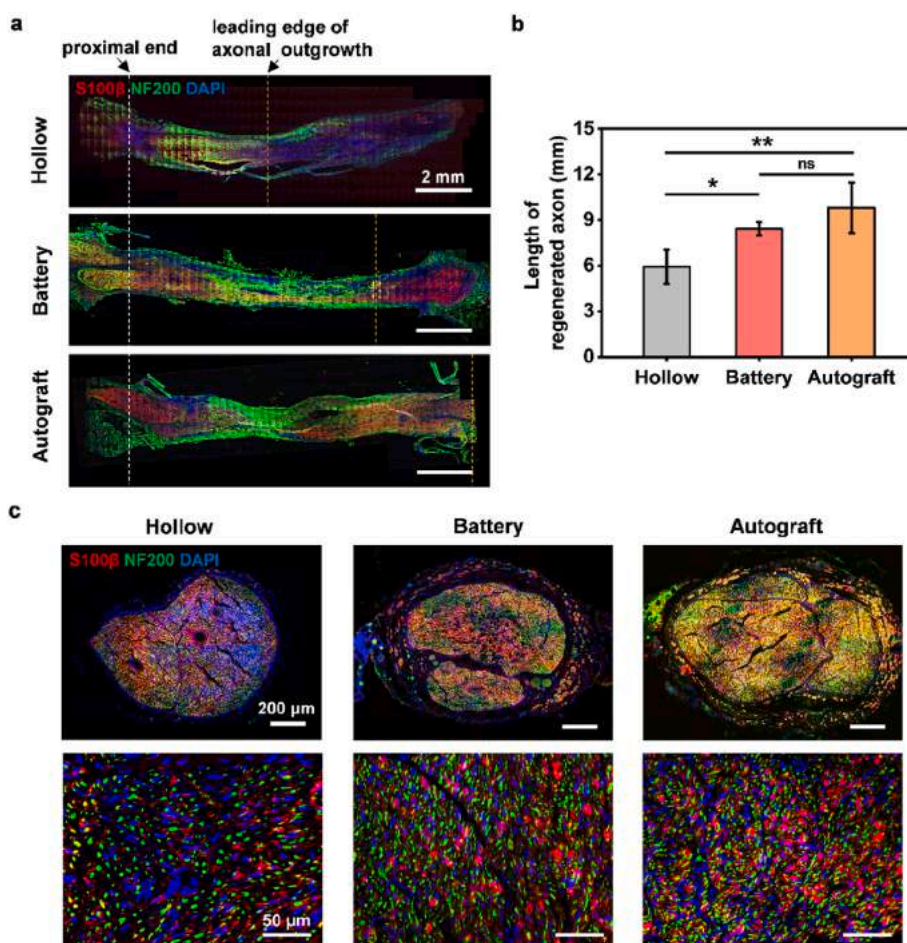

Fig. 3. Evaluation of sciatic nerve regeneration at 3 weeks and 12 weeks after implantation of hollow nerve conduits without the zinc-molybdenum battery (hollow group), self-powered NGCs (battery group) and autografts (autograft group) respectively. a. Immunofluorescent images of the longitudinal sections of regenerated nerve segments at 3 weeks postimplantation. **b.** Length of regenerated axons on week 3. In **a** and **b**, n = 3 individual animals for each group. **c.** Immunofluorescent images of the cross sections of regenerated nerves at the middle of the nerve segments at 12 weeks postimplantation. The upper is a full view of the regenerated tissue and the lower is corresponding magnified view. n = 5 individual animals for each group. Immunohistochemical staining: axons (NF200, green), Schwann cells (S100β, red), nuclei (DAPI, blue). The SPSS software package (version 27.0) was used for the statistical analysis, followed by one-way ANOVA (*P < 0.05, **P < 0.01).

mm), and statistically comparable to that of the autograft group (9.81 ± 1.66 mm), indicating the positive effects of the self-powered NGC integrating the zinc-molybdenum battery. Immunofluorescent images of transverse sections of regenerated nerve tissues at week 12 also indicate enhanced therapeutic outcomes in the battery and autograft groups compared to that of the hollow group (Fig. 3c). This improvement is evidenced by a greater density of regenerated axons and a more extensive positive area of S100β.

To investigate the myelination of regenerated nerves, toluidine blue staining and TEM characterization are performed at 12 weeks postoperatively. Representative results of toluidine blue staining are given in Fig. 4a, and the statistical analysis of the density of myelinated nerve fibers is shown in Fig. 4c. The number of regenerated myelinated nerve

fibers in the battery group are significantly greater than that in the hollow group (p < 0.05) and lower than that in the autograft group (p < 0.05). The microstructure of myeline sheath and regenerated nerve fibers is observed by TEM (Fig. 4b), and corresponding statistical results are given in Fig. 4d–f. As shown in Fig. 4d, the diameter of myelinate nerve fibers of the battery group (5.33 ± 1.55 μm) is comparable to that of the autograft group (5.08 ± 1.31 μm), and is significantly greater (p < 0.05) than that in the hollow group (4.08 ± 1.10 μm), indicating a greater axonal maturity. Moreover, the thickness of myelin sheath is significantly greater (p < 0.001) in the battery group (1.30 ± 0.30 μm) and autograft groups (1.19 ± 0.32 μm) than that in the hollow group (0.76 ± 0.17 μm, Fig. 4e). The g-ratio is an index reflecting the degree of axonal myelination calculated by dividing the area of axons by the area
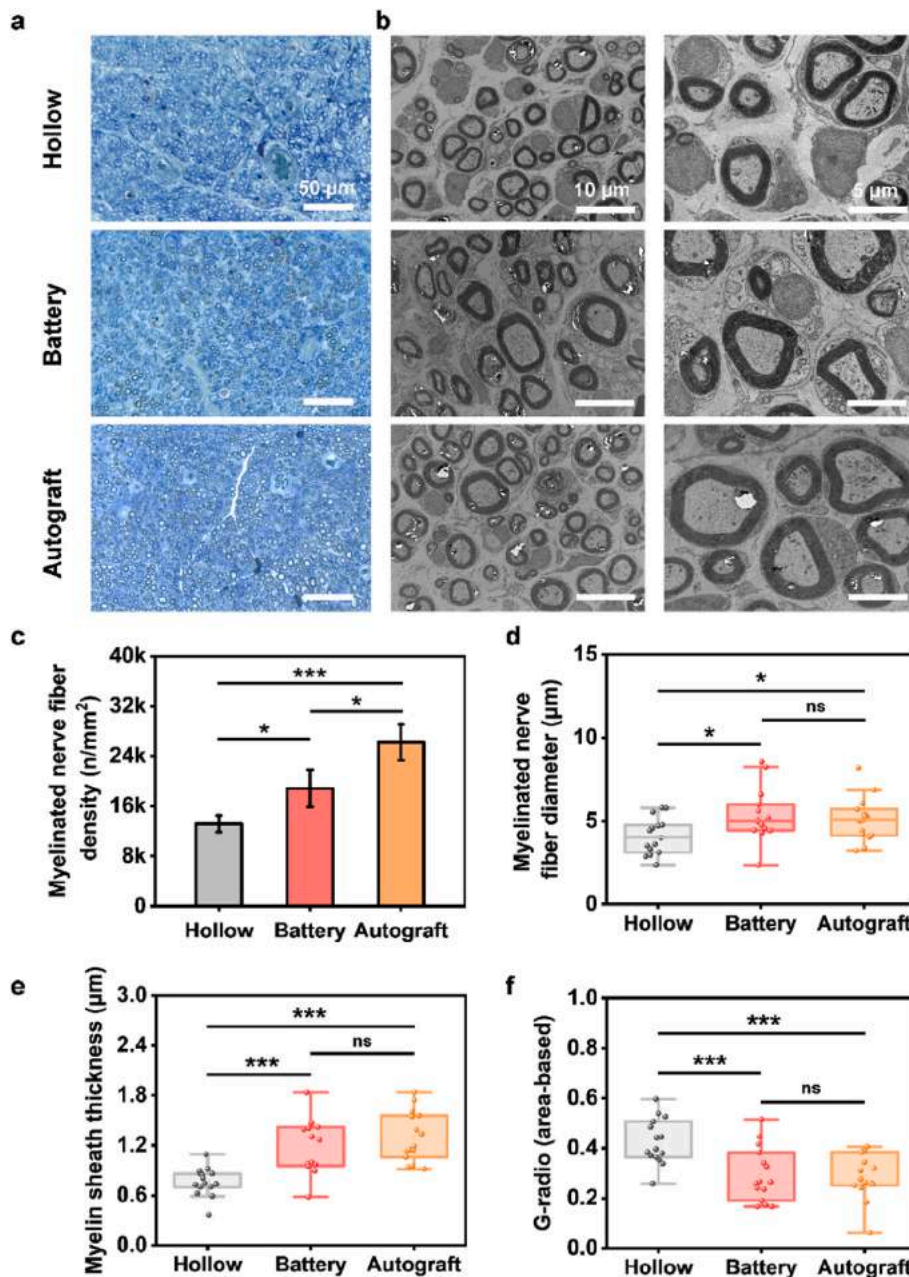

Fig. 4. Evaluation of regenerated nerve fibers at 12 weeks postimplantation of hollow nerve conduits, self-powered NGCs and autografts respectively. a. Toluidine Blue staining of the cross sections of regenerated nerve segments at the distal end. **b.** TEM images of the cross sections of regenerated nerve segments at the distal end. **c.** Myelinated nerve fiber density of regenerated nerve. **d.** Average diameter of myelinated nerve fiber. **e.** Average thickness of myelin sheath. **f.** Average area-based g-radio. n = 5 individual animals for each group. The SPSS software package (version 27.0) was used for the statistical analysis, followed by one-way ANOVA (*P < 0.05, ***P < 0.001).

of the myelinated nerve fibers. Results show that the g-ratio of the battery group (0.29 ± 0.11) is comparable to that of the autograft group (0.29 ± 0.09), and is significantly smaller (p < 0.001) than that of the hollow group (0.43 ± 0.09), indicating a greater myelination. These results collectively suggest the introduction of the self-powered NGC provides a positive effect on the myelination of regenerated nerve fibers. Results of H&E staining indicates no significant inflammations after 12 weeks of implantation (Fig. S4b).

3.4. Function recovery with the self-powered NGC

The therapeutic effects of the self-powered NGC on motor function recovery are investigated by electrophysiological testing, gastrocnemius muscle assessment and gait analysis. Electrophysiological studies are performed at 12 weeks postimplantation to assess the recovery of nerve conduction. Electrical stimulation of 0.3 mA and 200 μs is applied to the proximal site of the injured nerve and the CMAP is measured at the
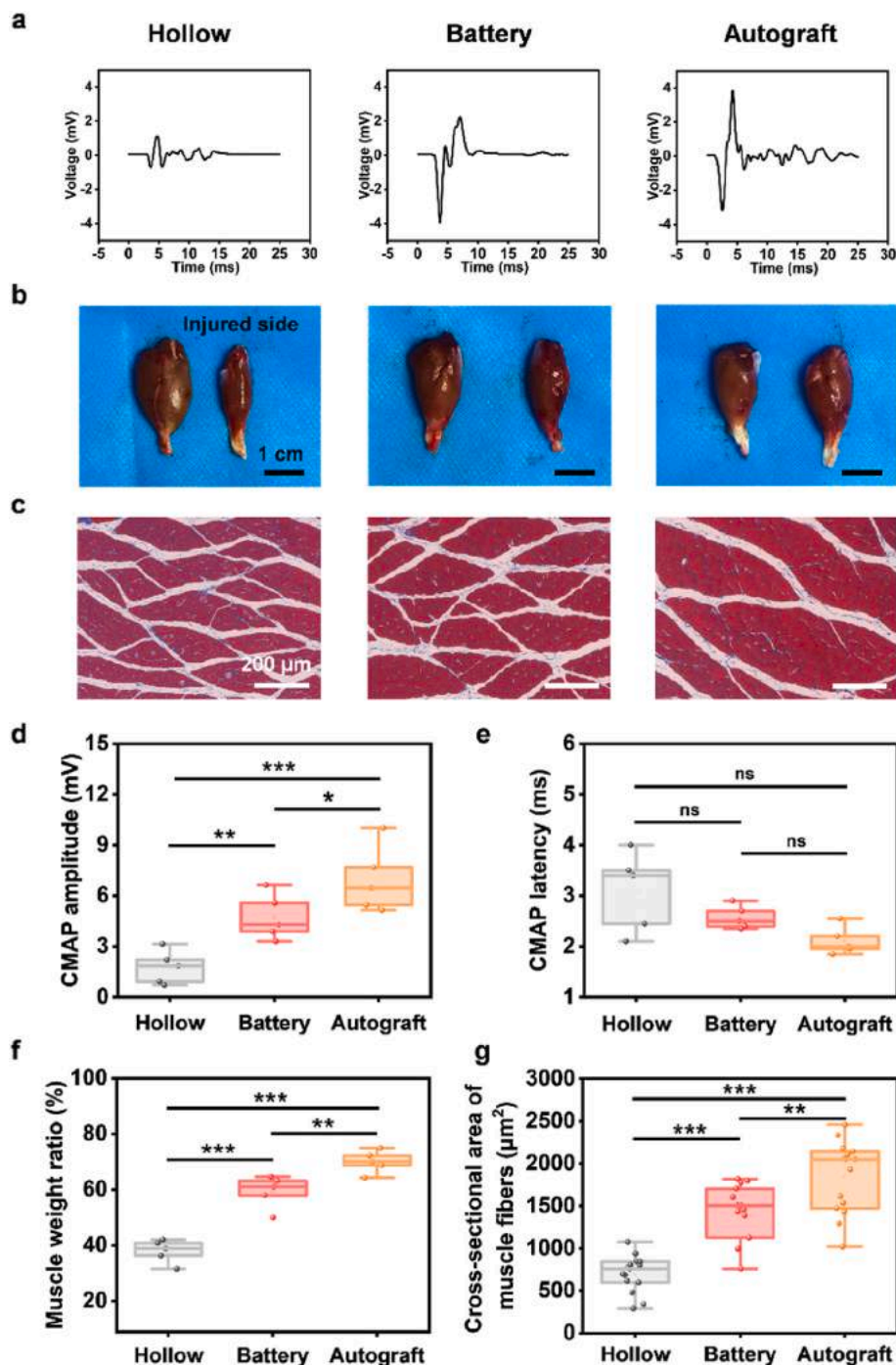

Fig. 5. Evaluation of gastrocnemius muscles at 12 weeks postimplantation of hollow nerve conduits, self-powered NGCs and autografts respectively. a. Representative waves of compound motor action potential at the injured side. Electrical stimulation: 0.3 mA, 0.2 ms. **b.** Representative gross images of the isolated gastrocnemius muscles of the injured side (right) and the contralateral side (left). **c.** Masson's trichrome staining images of the cross section of gastrocnemius muscles of the injured side. **d.** Average CMAP amplitude at the injured side. **e.** Average CMAP latency at the injured side. **f.** Wet weight ratio of the gastrocnemius muscles from the injured side. **g.** Cross-sectional area of muscle fibers at the injured side. n = 5 individual animals for each group. The SPSS software package (version 27.0) was used for the statistical analysis, followed by one-way ANOVA (**P < 0.01, ***P < 0.001).

target gastrocnemius muscle. The representative CMAP are given in Fig. 5a. The amplitude and latency of CMAP are statistically analyzed to assess the functional reconstruction of the innervated muscle (Fig. 5d and e). The results show a significantly greater (p < 0.01) CMAP amplitude of the battery group (4.74 ± 1.35 mV) than that of the hollow group (1.77 ± 0.99 mV), indicating that more regenerated motor units and innervated muscle fibers are achieved by the self-powered NGC. The CMAP amplitude of the autograft group (6.95 ± 1.98 mV) is significantly greater than the other two groups (p < 0.05 and p < 0.001). In addition, no significant difference in CMAP latency is observed among the battery group, the autograft group and the hollow group (Fig. 5e).

Sciatic nerve injury often results in the atrophy of innervated target muscles until they are reinnervated by regenerated nerves. The degree of

gastrocnemius muscle atrophy is an important index of motor function recovery, which is evaluated by muscle wet weight and Masson's staining at 12 weeks postoperatively. The representative gross images of the gastrocnemius muscle are shown in Fig. 5b, with the injured side on the right and the contralateral side on the left. The wet weight ratio of the battery group is significantly greater than that of the hollow group (p < 0.001) and smaller than that of the autograft group (p < 0.01) (Fig. 5f). Masson's trichrome staining is a histological way to visualize muscle tissues and collagen fibers. Representative images of Masson's staining are given in Fig. 5c and the average area of muscle fibers are analyzed and the results are given in Fig. 5g. The results indicate a significantly greater area of muscle fibers in the battery group (1425 ± 322 μm^2) and the autograft group (1846 ± 420 μm^2), than that of the
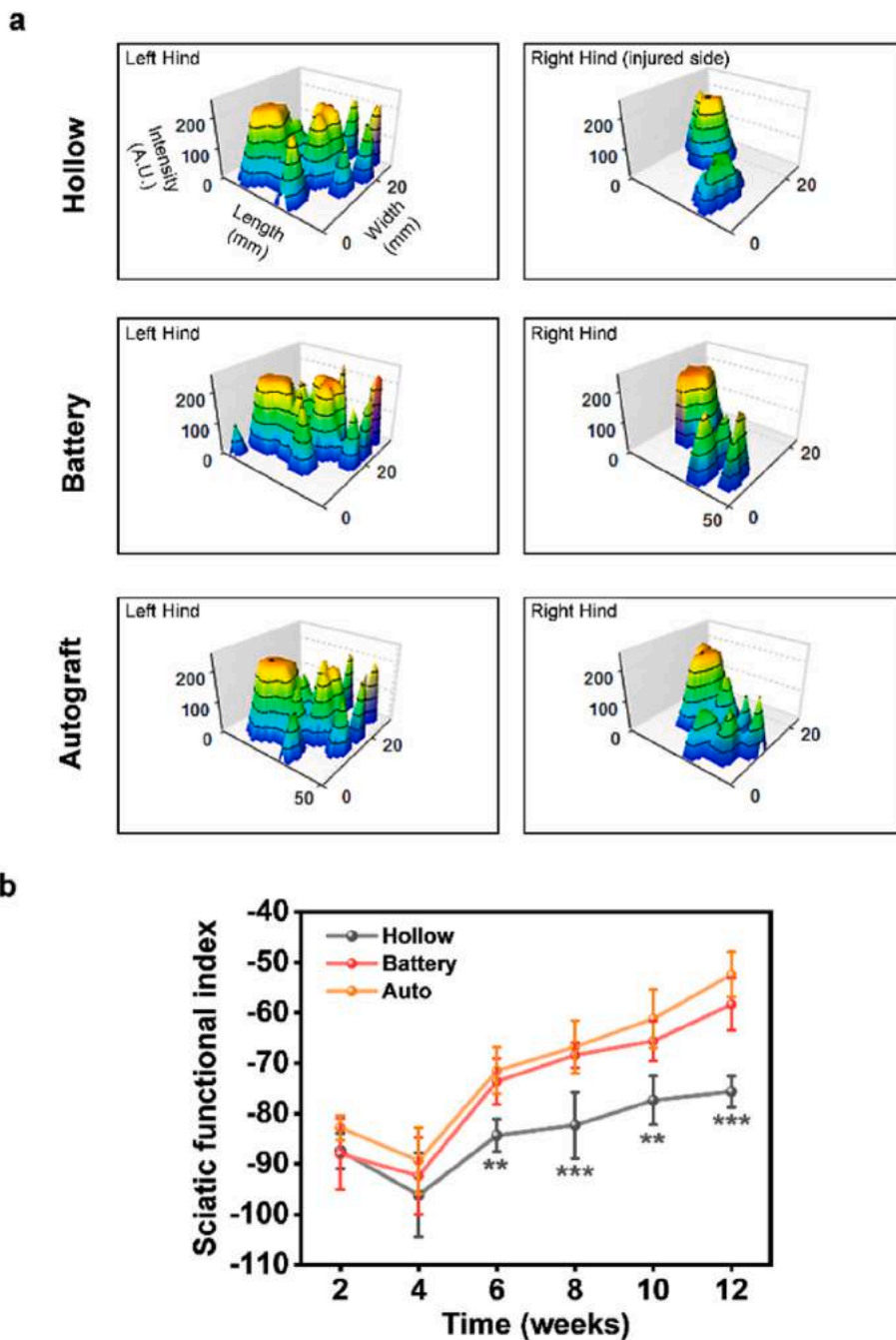

Fig. 6. Evaluation of motor functional recovery of hollow, battery and autograft groups. a. Representative 3D plantar pressure distribution of walking tack of SD rats at 12 weeks postoperatively. A.U., arbitrary units. **b.** Sciatic functional index of SD rats at 2, 4, 6, 8, 10, 12 weeks postoperatively. n = 5 individual animals for each group. The SPSS software package (version 27.0) was used for the statistical analysis, followed by one-way ANOVA (**P < 0.01, ***P < 0.001).

hollow group ($704 \pm 212\ \mu m^2$) (p < 0.001). Less collagenous deposits are also found in the battery and autograft group. These results indicate the beneficial effects of the introduction of the self-powered NGC on gastrocnemius muscle reinnervation.

Furthermore, gait analysis is carried out every two weeks postoperatively to monitor the recovery of motor functions. The 2D toe imprints and 3D plantar pressure distribution is recorded and analyzed. Representative images of 3D footprints of hind limbs are shown in Fig. 6a, with the injured side on the right and the contralateral side on the left. The x-axis and y-axis represent the length and width of footprints, while the z-axis reflects the relative plantar pressure. The SFI calculated by the footprints is a measure for the functional recovery of the sciatic nerve, where the closer it is to 0, the better motor functions recover. The SFI decreases in the first four weeks after surgery and there is no significant difference among three groups. This is probably because the reinnervation to target muscles has not been established at the early stage. The SFI of the battery and autograft group increases significantly at the week 6, and exhibits continuous improvement. There is no significant difference between the battery and autograft groups at 12 weeks postoperatively (Fig. 6b), and they are both greater compared with the control group (p < 0.001). The results of gait analysis indicate an improved motor function recovery accomplished by the self-powered NGC, which could be attributed to the faster elongation of regenerated axons and the enhanced innervated muscle fibers and regenerated motor units. Collectively, the in vitro and in vivo results show that the electrical cues provided by the zinc-molybdenum batteries can significantly promote the proliferation and ATP production of Schwann cells, thus could facilitate the regrowth of neurites and myelination, which accelerates the reinnervation of target muscle and the restoration of motor functions.

4. Conclusion

We propose a fully biodegradable and self-powered NGC based on zinc-molybdenum batteries for peripheral nerve regeneration, which can offer both topographic guidance as well as continuous electric cues. The device is miniaturized and easily deployable without the dependence on external equipment, and it is fully biodegradable, avoiding the risk of a secondary surgery for device retrieval. Zinc-molybdenum batteries demonstrate desirable biocompatibility and functionality for peripheral nerve repair, including the improvement of Schwann cell proliferation and ATP production, and the acceleration of axon growth, myelination and motor function recovery in the cases of sciatic nerve defects in rodents. Further optimization includes reducing the wall thickness and improving the permeability of the conduit. For the creation of biomimetic microenvironments using optimized electric fields and to achieve maximum therapeutic effects, future research could focus on investigating battery systems that offer controllable and further extended degradation time frames and various output modes. This study puts forth a biodegradable NGC that utilize zinc batteries to provide sustained electric fields for treating nerve defects, presenting promising prospects for the advancement of regenerative medicine and neuromodulation.

CRediT authorship contribution statement

Bingbing Yu: Writing – original draft, Methodology, Investigation, Formal analysis, Data curation. **Jun Bai:** Writing – original draft, Methodology, Data curation. **Yanjun Guan:** Writing – original draft, Methodology, Data curation. **Xueying Huang:** Investigation, Conceptualization. **Lijing Liang:** Methodology, Data curation. **Zhiqi Ren:** Methodology. **Xiangyu Song:** Methodology. **Tieyuan Zhang:** Methodology. **Can Yang:** Methodology. **Fanqi Dai:** Methodology. **Xibo Wang:** Investigation. **Xing Sheng:** Writing – review & editing, Resources. **Jiang Peng:** Writing – review & editing, Supervision, Resources. **Liu Wang:** Writing – review & editing, Validation, Supervision, Formal analysis,

Resources. **Yu Wang:** Writing – review & editing, Supervision, Project administration, Resources. **Lan Yin:** Writing – review & editing, Project administration, Conceptualization, Resources.

Declaration of competing interest

The authors declare no competing interests.

Data availability

Data will be made available on request.

Appendix A. Supplementary data

Supplementary data to this article can be found online at https://doi.org/10.1016/j.bios.2024.116578.

References

Adams, R.D., Gupta, B., Harkins, A.B., 2017. J. Neurophysiol. 118 (2), 1415–1424.

Bai, J., Yu, B., Li, C., Cheng, H., Guan, Y., Ren, Z., Zhang, T., Song, X., Jia, Z., Su, T., Tao, B., Gao, H., Yang, B., Liang, L., Xiong, X., Zhou, X., Yin, L., Peng, J., Shang, A., Wang, Y., 2023. Adv. Healthcare Mater. 13 (3), e2302128.

Carthew, R.W., 2021. Trends Genet. 37 (4), 389–400.

Carvalho, C.R., Oliveira, J.M., Reis, R.L., 2019. Front. Bioeng. Biotechnol. 7 (337), 1.

Casella, A., Panitch, A., Leach, J.K., 2021. Bioelectricity 3 (1), 27–41.

Choi, Y.S., Hsueh, Y.Y., Koo, J., Yang, Q., Avila, R., Hu, B., Xie, Z., Lee, G., Ning, Z., Liu, C., Xu, Y., Lee, Y.J., Zhao, W., Fang, J., Deng, Y., Lee, S.M., Vazquez-Guardado, A., Stepien, I., Yan, Y., Song, J.W., Haney, C., Oh, Y.S., Liu, W., Yoon, H. J., Banks, A., MacEwan, M.R., Ameer, G.A., Ray, W.Z., Huang, Y., Xie, T., Franz, C.K., Li, S., Rogers, J.A., 2020. Nat. Commun. 11 (1), 5990.

Chu, X.L., Song, X.Z., Li, Q., Li, Y.R., He, F., Gu, X.S., Ming, D., 2022. Neural Regen Res 17 (10), 2185–2193.

Di Pietro, M.E., Mele, A., 2021. J. Mol. Liq. 338, 116597.

Díaz-Vegas, A., Eisner, V., Jaimovich, E., 2019. Arch. Biochem. Biophys. 664, 89–94.

Feinberg, J.H., Nadler, S.F., Krivickas, L.S., 1997. Sports Med. 24 (6), 385–408.

Frederick, R.A., Troyk, P.R., Cogan, S.F., 2021. IEEE Eng. Med. Biol. 6562–6564.

Gordon, T., 2016. Neurotherapeutics 13 (2), 295–310.

Gordon, T., English, A.W., 2016. Eur. J. Neurosci. 43 (3), 336–350.

Guo, H., D'Andrea, D., Zhao, J., Xu, Y., Qiao, Z., Janes, L.E., Murthy, N.K., Li, R., Xie, Z., Song, Z., Meda, R., Koo, J., Bai, W., Choi, Y.S., Jordan, S.W., Huang, Y., Franz, C.K., Rogers, J.A., 2021. Adv. Funct. Mater. 31 (29).

Huang, X., Wang, D., Yuan, Z., Xie, W., Wu, Y., Li, R., Zhao, Y., Luo, D., Cen, L., Chen, B., 2018. Small 14 (28), 1800994.

Huang, X., Hou, H., Yu, B., Bai, J., Guan, Y., Wang, L., Chen, K., Wang, X., Sun, P., Deng, Y., Liu, S., Cai, X., Wang, Y., Peng, J., Sheng, X., Xiong, W., Yin, L., 2023. ACS Nano 17 (6), 5727–5739.

Ino, D., Sagara, H., Suzuki, J., Kanemaru, K., Okubo, Y., Iino, M., 2015. Cell Rep. 12 (12), 1951–1959.

Institute of Medicine Panel on M, 2001. Dietary Reference Intakes for Vitamin A, Vitamin K, Arsenic, Boron, Chromium, Copper, Iodine, Iron, Manganese, Molybdenum, Nickel, Silicon, Vanadium, and Zinc. National Academies Press (US) Copyright 2001 by the National Academy of Sciences. All rights reserved, Washington (DC).

Isaacson, B.M., Bloebaum, R.D., 2010. J. Biomed. Mater. Res. 95A (4), 1270–1279.

Jayasayee, K., Clark, S., King, C., Dahl, P.I., Richard Tolchard, J., Juel, M., 2020. Processes 8 (5), 592.

Jin, F., Li, T., Yuan, T., Du, L., Lai, C., Wu, Q., Zhao, Y., Sun, F., Gu, L., Wang, T., Feng, Z. Q., 2021. Adv. Mater. 33 (48), e2104175.

Jing, W., Zhang, Y., Cai, Q., Chen, G., Wang, L., Yang, X., Zhong, W., 2019. ACS Chem. Neurosci. 10 (1), 348–357.

Johnson, E.O., Soucacos, P.N., 2008. Injury 39 (3), 30–36.

Kemp, S.W.P., Cederna, P.S., Midha, R., 2017. Exp. Neurol. 287, 348–357.

Kong, J., Teng, C., Liu, F., Wang, X., Zhou, Y., Zong, Y., Wan, Z., Qin, J., Yu, B., Mi, D., Wang, Y., 2024. Front. Neurosci. 18.

Koo, J., MacEwan, M.R., Kang, S.K., Won, S.M., Stephen, M., Gamble, P., Xie, Z., Yan, Y., Chen, Y.Y., Shin, J., Birenbaum, N., Chung, S., Kim, S.B., Khalifeh, J., Harburg, D.V., Bean, K., Paskett, M., Kim, J., Zohny, Z.S., Lee, S.M., Zhang, R., Luo, K., Ji, B., Banks, A., Lee, H.M., Huang, Y., Ray, W.Z., Rogers, J.A., 2018. Nat. Med. 24 (12), 1830–1836.

Koppes, A.N., Seggio, A.M., Thompson, D.M., 2011. J. Neural. Eng. 8 (4).

Koppes, A.N., Nordberg, A.L., Paolillo, G.M., Goodsell, N.M., Darwish, H.A., Zhang, L., Thompson, D.M., 2014. Tissue Eng. 20 (3–4), 494–506.

Lee, Y.K., Kim, J., Kim, Y., Kwak, J.W., Yoon, Y., Rogers, J.A., 2017. Adv. Mater. 29 (38), 1702665.

Lee, G.M., Ray, E., Yoon, H.J., Genovese, S., Choi, Y.S., Lee, M.K., Sahin, S., Yan, Y., Ahn, H.Y., Bandodkar, A.J., Kim, J., Park, M., Ryu, H., Kwak, S.S., Jung, Y.H., Odabas, A., Khandpur, U., Ray, W.Z., MacEwan, M.R., Rogers, J.A., 2022. Sci. Adv. 8 (40).

Lei, S., Liu, Z., Liu, C., Li, J., Lu, B., Liang, S., Zhou, J., 2022. Energy Environ. Sci. 15 (12), 4911–4927.

Li, X., Zhang, T., Li, C., Xu, W., Guan, Y., Li, X., Cheng, H., Chen, S., Yang, B., Liu, Y., Ren, Z., Song, X., Jia, Z., Wang, y, Tang, J., 2022. Glia 71.

Li, L., Li, D., Wang, Y., Ye, T., He, E., Jiao, Y., Wang, L., Li, F., Li, Y., Ding, J., Liu, K., Ren, J., Li, Q., Ji, J., Zhang, Y., 2023. Adv. Mater., e2302997

Li, C., Luo, R., Bai, Y., Shao, J., Ji, J., Wang, E., Li, Z., Meng, H., Li, Z., 2024. Adv. Funct. Mater. 34 (29), 2400277.

Lu, C., Wang, Y., Yang, S., Wang, C., Sun, X., Lu, J., Yin, H., Jiang, W., Meng, H., Rao, F., Wang, X., Peng, J., 2018. ACS Biomater. Sci. Eng. 4 (8), 2994–3005.

Mao, R., Yu, B., Cui, J., Wang, Z., Huang, X., Yu, H., Lin, K., Shen, S.G.F., 2022. Nano Energy 98.

Mar, F.M., Bonni, A., Sousa, M.M., 2014. EMBO Rep. 15 (3), 254–263.

McLean, N.A., Verge, V.M., 2016. Glia 64 (9), 1546–1561.

Meena, P., Kakkar, A., Kumar, M., Khatri, N., Nagar, R.K., Singh, A., Malhotra, P., Shukla, M., Saraswat, S.K., Srivastava, S., Datt, R., Pandey, S., 2021. Cell Tissue Res. 383 (2), 617–644.

Meng, S., 2014. Tissue Engineering and Regenerative Medicine 11 (4), 274–283.

Meng, H., Yu, Q., Liu, Z., Gai, Y., Xue, J., Bai, Y., Qu, X., Tan, P., Luo, D., Huang, W., Nie, K., Bai, W., Hou, Z., Tang, R., Xu, H., Zhang, Y., Cai, Q., Yang, X., Wang, Z.L., Li, Z., 2023. Matter 6 (12), 4274–4290.

Monk, K.R., Feltri, M.L., Taveggia, C., 2015. Glia 63 (8), 1376–1393.

Noble, J., Munro, C.A., Prasad, V.S., Midha, R., 1998. J. Trauma 45 (1), 116–122.

Sun, Y., Quan, Q., Meng, H., Zheng, Y., Peng, J., Hu, Y., Feng, Z., Sang, X., Qiao, K., He, W., Chi, X., Zhao, L., 2019. Adv. Healthcare Mater. 8 (10), e1900127.

Shan, Y., Wang, E., Cui, X., Xi, Y., Ji, J., Yuan, J., Xu, L., Liu, Z., Li, Z., 2024. Adv. Funct. Mater., 2400295

Sun, P., Li, C., Yang, C., Sun, M., Hou, H., Guan, Y., Chen, J., Liu, S., Chen, K., Ma, Y., Huang, Y., Li, X., Wang, H., Wang, L., Chen, S., Cheng, H., Xiong, W., Sheng, X., Zhang, M., Peng, J., Wang, S., Wang, Y., Yin, L., 2024. Nat. Commun. 15 (1).

Taylor, C.A., Braza, D., Rice, J.B., Dillingham, T., 2008. Am. J. Phys. Med. Rehab. 87 (5), 381–385.

Wan, L., Zhang, S., Xia, R., Ding, W., 2010. J. Neurosci. Res. 88 (12), 2578–2587.

Wang, L., Lu, C., Yang, S., Sun, P., Wang, Y., Guan, Y., Liu, S., Cheng, D., Meng, H., Wang, Q., He, J., Hou, H., Li, H., Lu, W., Zhao, Y., Wang, J., Zhu, Y., Li, Y., Luo, D., Li, T., Chen, H., Wang, S., Sheng, X., Xiong, W., Wang, X., Peng, J., Yin, L., 2020. Sci. Adv. 6 (50), eabc6686.

Wang, L., Chen, K., Fan, Y., Yin, L., 2022. Medicine in Novel Technology and Devices 16.

Xie, J., MacEwan, M.R., Liu, W., Jesuraj, N., Li, X., Hunter, D., Xia, Y., 2014. ACS Appl. Mater. Interfaces 6 (12), 9472–9480.

Yang, Y., Yin, X., Wang, H., Qiu, W., Li, L., Li, F., Shan, Y., Zhao, Z., Li, Z., Guo, J., Zhang, J., Zhao, Y., 2023. Nano Energy 107.

Yang, W., Yang, W., Zeng, J., Chen, Y., Huang, Y., Liu, J., Gan, J., Li, T., Zhang, H., Zhong, L., Peng, X., 2024. Prog. Mater. Sci. 144, 101264.

Yin, L., Huang, X., Xu, H., Zhang, Y., Lam, J., Cheng, J., Rogers, J.A., 2014a. Adv. Mater. 26 (23), 3879–3884.

Yin, L., Cheng, H., Mao, S., Haasch, R., Liu, Y., Xie, X., Hwang, S.W., Jain, H., Kang, S.K., Su, Y., 2014b. Adv. Funct. Mater. 24 (5), 645–658.

Yu, Q., Bai, Y., Li, Z., Jiang, F., Luo, R., Gai, Y., Liu, Z., Zhou, L., Wang, Y., Li, C., Ren, K., Luo, D., Meng, H., Li, Z., 2024. Nano Energy 121.

Zhao, Y., Liang, Y., Ding, S., Zhang, K., Mao, H-q, Yang, Y., 2020a. Biomaterials 255.

Zhao, Y., Liang, Y., Ding, S., Zhang, K., Mao, H-q, Yang, Y., 2020b. Biomaterials 255, 120164.

Zheng, Q., Zou, Y., Zhang, Y.L., Liu, Z., Shi, B.J., Wang, X.X., Jin, Y.M., Ouyang, H., Li, Z., Wang, Z.L., 2016. Sci. Adv. 2 (3).
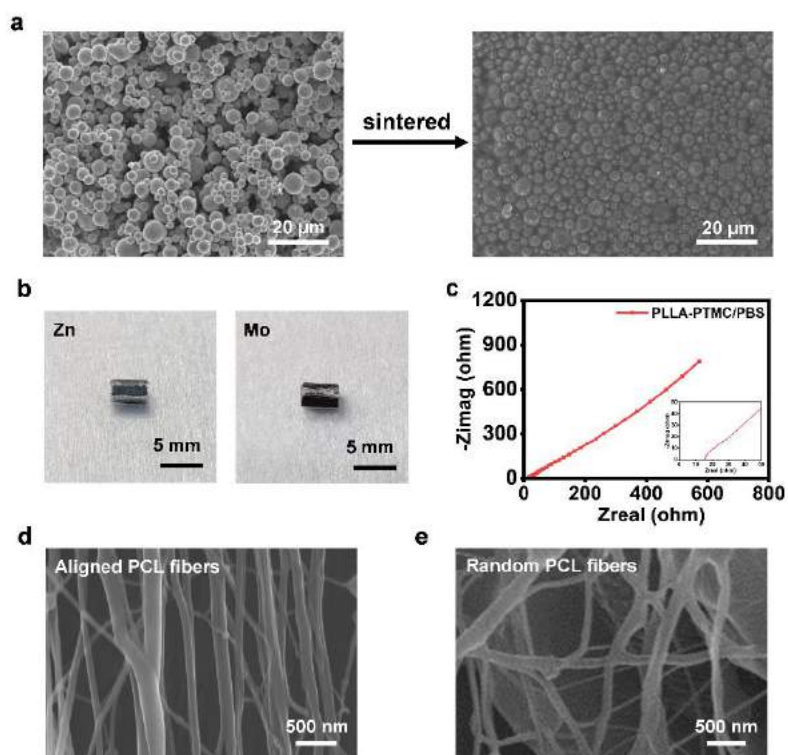
Supporting information

Figure S1. Characterization of the self-powered NGC. a. SEM images of zinc particles before and after room-temperature sintering. **b.** Optical images of separated zinc and molybdenum electrode in the self-powered NGC. **c.** Electrochemical impedance spectroscopy of PLLA-PTMC film (5 mm × 10 mm × 50 μm) soaked in PBS. **d.** Magnified SEM image of aligned PCL fibers for structural guidance. **e.** Magnified SEM image of randomly oriented PCL fibers for mechanical support.
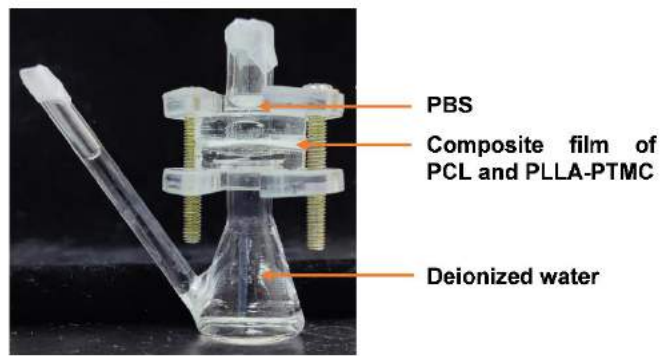
Figure S2. Evaluation of mass transportation of the multiple-layered device.
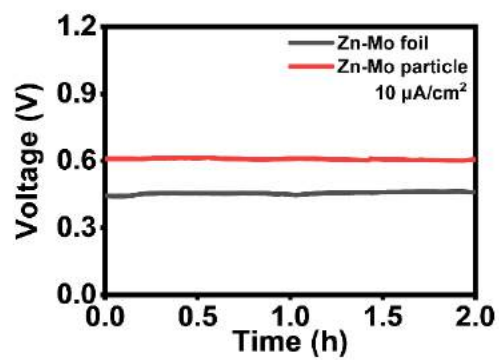
Figure S3. Comparison of discharge behavior of zinc-molybdenum battery based on metal foils and metal particles respectively, with a discharge current density of 10 µA/cm².
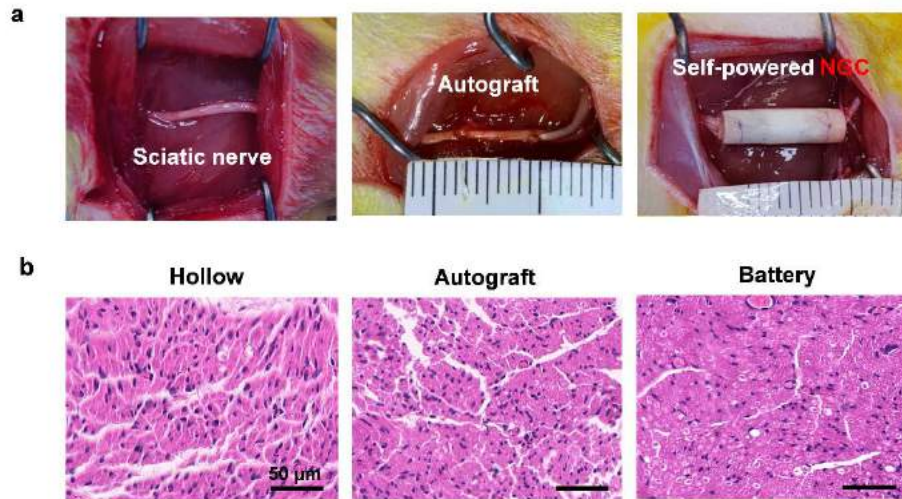
Figure S4. Characterization of the self-powered NGC. a. Surgical images of implantation. Images: native sciatic nerve (left), implanted autograft (middle), implanted self-powered NGC (right). **b.** H&E staining images of the transverse sections of regenerated tissues at the middle of nerve segments at 12 weeks postimplantation.